Electronic Supplementary Material (ESI) for Green Chemistry.

Green Synthesis of Magnesium Single Atom Catalyst from Spinacia oleracea-Chlorophyll Extracts for Sustainable Electrocatalytic Nitrate Reduction to Ammonia

Kanhai Kumar,[a] Pragyan Tripathi,[a] Gokul Raj,[a] Dova Kalyan,[b] Demudu Babu Gorle,[a] Nikhil George Mohan,[c] Surendra Kumar Makineni,[b] Kothandaraman Ramanujam,[c] Abhishek Kumar Singh,[a] and Karuna Kar Nanda [a,d,e]*

[a]*Materials Research Centre, Indian Institute of Science, Bangalore-560012, India. E-mail: nanda@iisc.ac.in.*

[b]*Materials Engineering, Indian Institute of Science, Bangalore-560012, India*

[c]*Department of Chemistry, Indian Institute of Technology, Madras-600 036, India*

[d]*Institute of Physics (IOP), Bhubaneshwar-751005, India.*

[e]*Homi Bhabha National Institute, Anushaktinagar, Mumbai – 400094, India*

Contents

1. Table of Comparisons 4
   1.1. Table of comparison of synthesis strategies of various single atom-based catalysts 4
   1.2. Table of comparison of recent reports for nitrate ion to ammonia production 6
2. SEM images and SEM-EDS mapping 8
3. TEM analysis 9
4. HAADF-STEM analysis and EDS elemental mapping 9
5. Particle size distribution for MgNxC850 11
6. XPS studies 12
7. FTIR studies of MgNxC650 and MgNxC850 13
8. Thermogravimetric analysis (TGA) 13
9. BET analysis 13
10. Electrochemical analysis 14
11. Concentration-dependent studies 14
12. Cyclic test studies 15
13. Time-dependent studies 15
14. Quantification of the ions from the Cathodic compartment 16
15. Product analysis and efficiency calculations 16
   15.1. UV- Visible spectroscopy 16
      15.1.1. Nessler's method 16
      15.1.2. Griess's reagent test for NO_2^- anion 16
   15.2. NMR spectroscopy 17
   15.3. Ion-exchange (IC) chromatography 17
16. Cyclic voltammetry (CV) and electrochemical double-layer capacitance (C_{dl}) determination 19
17. Mott-Schottky analysis 20
18. Scherrer's equation for particle size calculation 20
19. Computational Details 21
20. Experimental Procedures 27
   20.1. Selection of precursors and their respective roles in MgNxC catalyst synthesis 27
   20.2. Extraction of chlorophyll 28
   20.3. Analysis of Chlorophyll extract 29
   20.4. Physical filtration and selection of coffee powder 29
   20.5. Preparation of precursors 30

20.6. Mg-intermediate Processing: 31
20.7. Pyrolysis of Mg-intermediate 31
20.8. Catalysts chemical compositional analysis 32
21. Electrochemical measurements 33
References 34

1. Table of Comparisons

1.1. Table of comparison of synthesis strategies of various single atom-based catalysts

Table S1 (a). Synthesis strategies for various single atom-based catalysts

Synthesis methods	Merits	Demerits	Single metal atom-based catalysts	Reference
Atomic layer deposition	• Controllable size and dispersion of particles • uniformity and reproducibility	• High equipment cost • Low yield • Only materials with suitable ligands or functional groups could be chosen as support	Pt/graphene SAC Pd1Ni SAA	[1, 2]
Co-precipitation	• Simple and quick preparation • Low cost • Applicable for preparing composite oxides containing two or more uniformly dispersed metal elements	• Easy agglomeration • Low metal loading • Preparation parameters have a great impact on performance. • Some active atoms are not exposed and cannot participate in the reaction	Au1/CeO2 SAC and Au1/FeOx SAC Pt1/ZnO SAC and Au1/ZnO SAC Ir1/FeOx SAC	[3-5]
Co-impregnation	• Low cost • Simplest method • Varies metal choices	• Low yield • Generally, metal atoms are not uniformly dispersed on the surface of support	Pd-Ag/SiO2 _SeqIWI SAA and Pd-Ag/SiO2_CoIWI SAA Pt1/ATO (antimony doped tin–oxide) SAA	[6, 7]
Galvanic replacement	• Special compositions and structures • Simple, versatile	• Need difference between reduction potential between two metals. • Limited choices	Pd1Cu SAA, Pt1Cu SAA, and NiCu SAA. Pt/Cu SAAs Pt/Cu SAAs’	[8-10]
Ball-milling	• Simple, green, scalable production	• The catalysts are prone to agglomeration. • High maintenance • Time-consuming	FeN4/GN SAAs Pt1/Co SAAs Au1/CeO2 SAAs	[11-13]
Ion-exchange method	• high loadings of single atoms on the surface of a support.	• limited types of SACs can be synthesized.	Au alloyed Pd SAC	[14-16]
Thermal transformation	• Suitable large-scale production • Easy to anchor heteroatoms	• High-temperature maintenance • Time-consuming	Co SAs/N-C, Co NPs-N/C, and Pt/C Ni SAs/N-C and Ni NPs/N-C	[15, 17]

Table S1 (b). Synthesis strategies for various Magnesium single atom-based catalysts

Synthesis methods	Merits	Demerits	Single metal atom-based catalysts	Reference
Pre-doped to Mg-based MOFs followed by high-temperature pyrolysis	• The modified methods could be used for Aluminum and calcium. •	• 900 °C under Ar atmosphere • HMT is hazardous and can create irritation to the eye, skin, and respiratory systems	Mg–N–C	[18]
In-situ confinement high-temperature pyrolysis strategy	• An MOF-free approach for the synthesis of Mg-N-C based single atom catalyst.	• 800°C • Phthalimide is hazardous and potentially can create irritation to the eye, skin, and respiratory tract.	Mg-N-C/800	[19]
Sublimation-migration-anchoring (SMA) strategy	• Efficient for the preparation of Mg single-atom catalysts	• 650-680 °C • Preparation parameters have a great impact on performance. • Highly temperature-sensitive synthesis route	Mg1/G	[20]
Thermally assisted green route	• Green leaves have been utilized. • Environmentally friendly • Cost-effective • Non-toxic procedure • Single step pyrolysis • No hazardous solvent used.	• The temperature of 650 °C. • Chlorophyll extracted from leaves can differ among various green plants	MgNxC (Mg SAC)	This work

1.2. Table of comparison of recent reports for nitrate ion to ammonia production

Table S2. Table of comparison of recent reports for nitrate ion to ammonia production

	Catalysts	Electrolytic medium	F.E. (%)	Partial Current density (NH_3)	Production rate	Ref
1	Ti foil	0.4 M [NO_3^-] at pH ~ 0.77 (acidic)	82% at −1 V vs RHE	-0.77 22 $mA.cm^{-2}$	-	[21]
2	TiO_{2-X}	3.6 mM NO_3^-, 0.5 M $NaSO_4$	85%-at 0.556 V vs RHE	-	0.045 mmol $mg^{-1}_{cat.}$ h^{-1}	[22]
3	Copper-nickel alloys	100 mM NO_3^-, 1 M KOH, pH 14, -0.1 V vs RHE	99%	-90 $mA.cm^{-2}$	-	[23]
4	Strained Ru nanoclusters	1 M NO_3^-, 1 M KOH, -0.2 V versus RHE	~100%	-120 $mA.cm^{-2}$	5.56 mol g_{cat}^{-1} h^{-1} (1.17 mmol h^{-1} cm^{-2})	[24]
5	NiAlMnCoCu alloy	0.5 M KOH + 0.25 M KNO_3, −1.2 V versus SCE	~90%	4.61 $mA.cm^{-2}$	-	[25]
6	Cu/Cu2O NWAs	14.3 mM NO_3^-, 0.5 M $NaSO_4$, -0.85 V vs RHE	95.8%	-	0.2449 mmol h^{-1} cm^{-2}	[26]
7	Fe single-atom catalyst (SAC	0.5 M KNO_3/0.1 M K_2SO_4, (-0.66V) vs RHE	74.9	98.6 $mA.cm^{-2}$	0.46 mmol h^{-1} cm^{-2}	[27]
8	Co_3O_4@NiO	200 ppm NO_3^- + 0.5 M Na_2SO_4, -0.7 V vs RHE	54.97	-	0.00693 mmol h^{-1} mg^{-1}	[28]
9	Pd (111)	0.1 M NO_3^- + 0.1 M Na_2SO_4, -0.7 V RHE	79.91	-	0.5485 mmol h^{-1} cm^{-2}	[29]

10	Ni1Cu-Single atom alloy	0.5 M K2SO4 + 200 ppm NO_3- at – 0.55 V vs (RHE)	~100%	-	326.7 µmol h^{-1} cm^{-2}	[30]
11	Au/C	1.0 mM NO_3^- + 0.5 M K_2SO_4, -0.3 V RHE	26	-	0.00158 mmol h^{-1} cm^{-2}	[31]
12	a-RuO2	200 ppm NO_3^- + 0.5 M Na_2SO_4, -0.35 V vs RHE	97.46	-	0.1158 mmol h^{-1} cm^{-2}	[32]
13	SN Co-Li+ /PCNF	0.5 M NO_3^- + 0.5 M Na_2SO_4, -0.94V vs RHE	72.7	125.6 $mA.cm^{-2}$	0.71 mmol h^{-1} cm^{-2}	[33]
14	Ni SAC	0.50 M KNO_3 + 0.10 M K_2SO_4 at -0.82V vs RHE	69.8%	-	-	[27]
15	Co SAC	0.50 M KNO_3 + 0.10 M K_2SO_4	70.4% at -0.74V vs RHE	-	-	[27]
16	Cu/TiO2–x	–0.75 V vs RHE	81.34%	-	0.1143 mmol h^{-1} mg^{-1}	[34]
17	CoO@NCNT/GP	0.1 M NaOH + 0.1 M NO_3^- at -0.6V vs RHE	93.8 ± 1.5%	-	9041.6 ± 370.7 µg h^{-1} cm^{-2}	[35]
18	MgNxC650 (Mg SAC)	1M KOH + 1M KNO_3	81.5±2.9% at -0.58 V vs RHE	40 mA cm^{-2}	392.5±41.2 µmol h-1 mg-1 cat.	This work

2. SEM images and SEM-EDS mapping

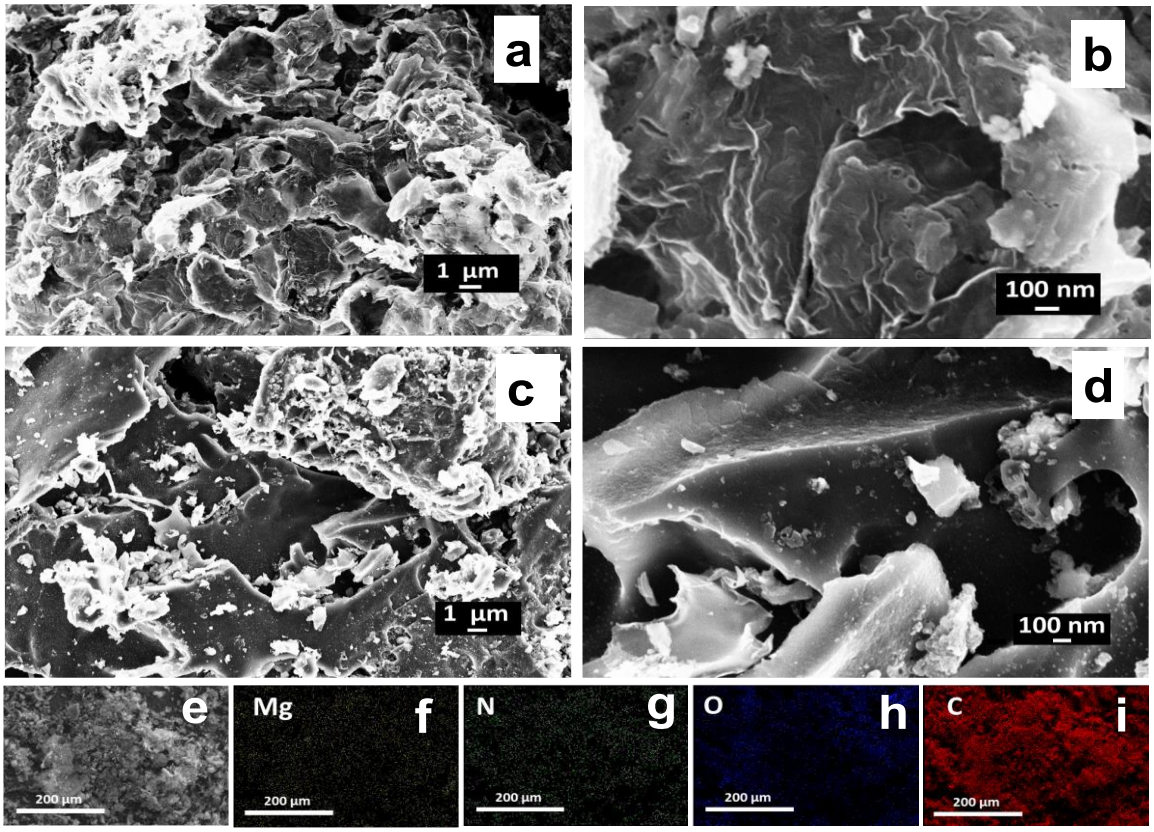

Figure. S1. SEM images of MgNxC650 (a-b), MgNxC850 (c-d) and different magnifications and EDS mapping of MgNxC650 with (e) selected region, (f-i) for Mg, N, O, and C, respectively.

3. TEM analysis

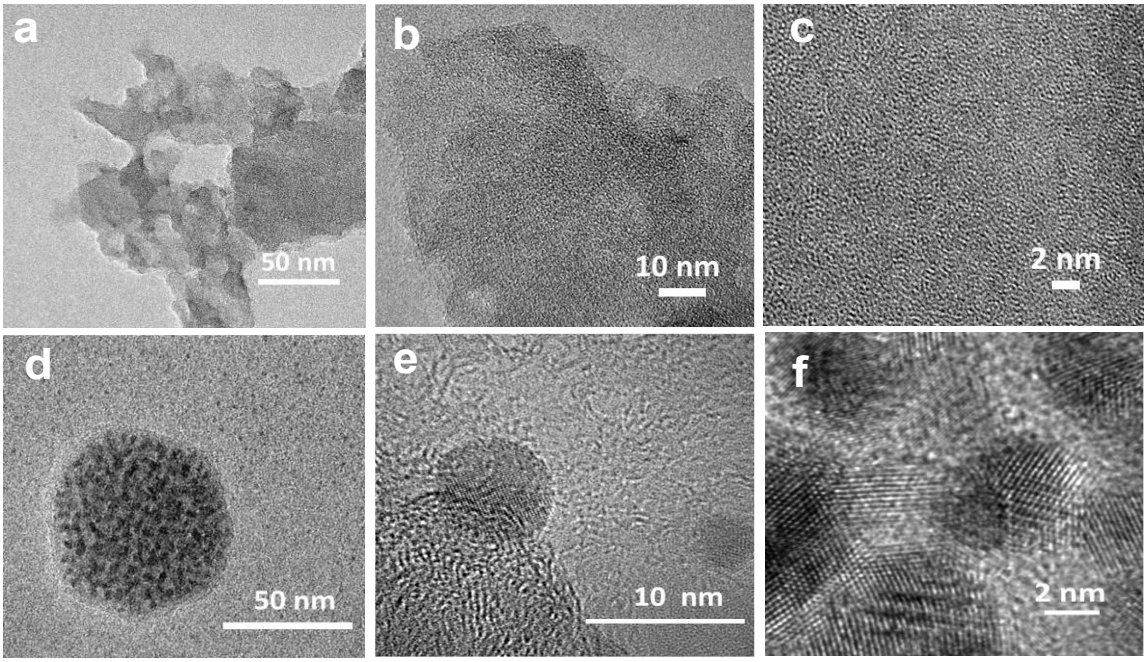

Figure. S2. HRTEM images at different magnifications of (a-c) MgNxC650 and (d-f) MgNxC850.

4. HAADF-STEM analysis and EDS elemental mapping

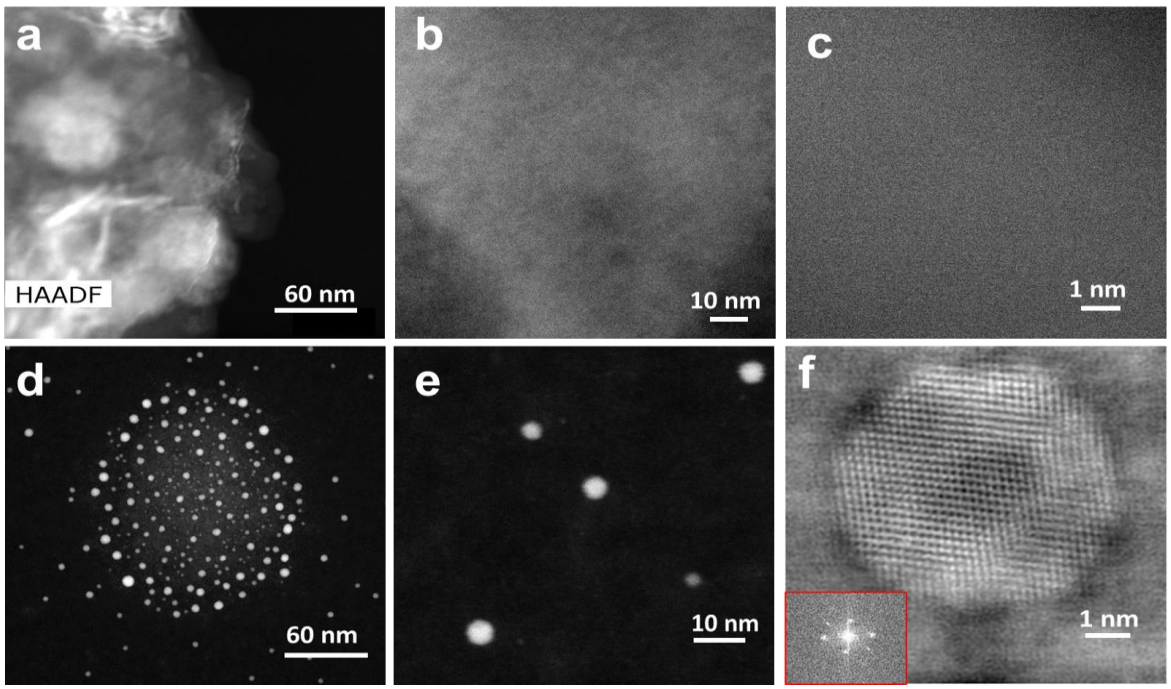

Figure. S3. HAADF-STEM EDS imaging of (a-c) MgNxC650, and (d-f) MgNxC850.

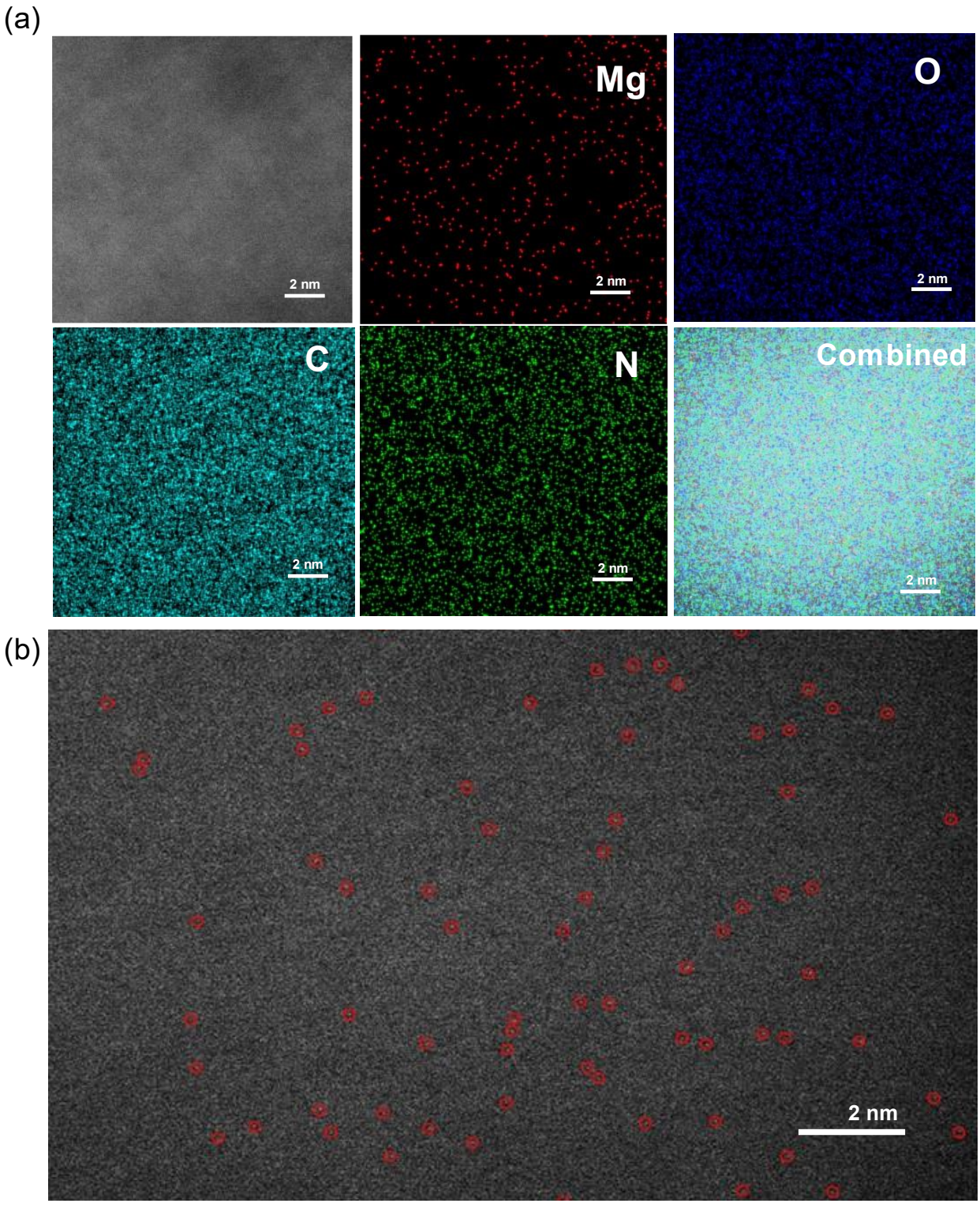

Figure. S4. (a) Elemental mapping of elements, and (b) atomic dispersion of magnesium atoms of MgNxC650.

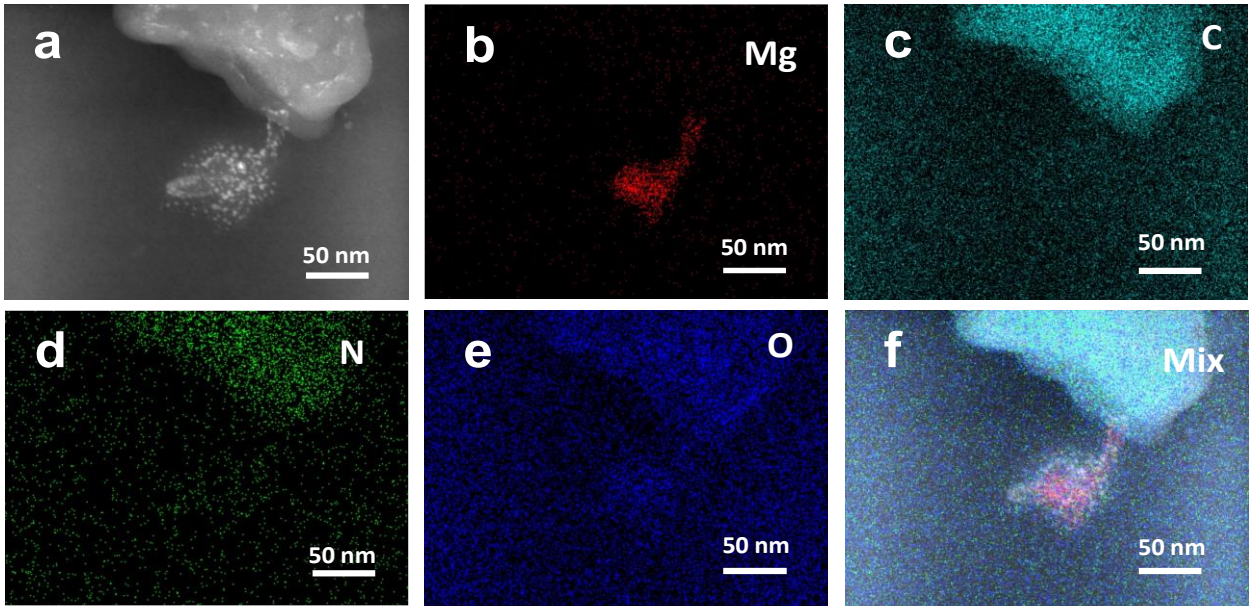

Figure. S5. HAADF-STEM EDS elemental mapping of MgNxC850 (a) region of interest, (b) Mg, (c) C, (d) N, (e) O, and (f) mixed depiction of the distribution of respective elements.

5. Particle size distribution for MgNxC850

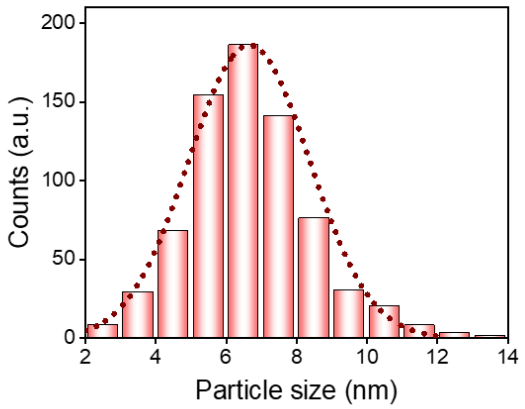

Figure. S6. Particle size distribution of nanoparticle in MgNxC850 catalyst.

6. XPS studies

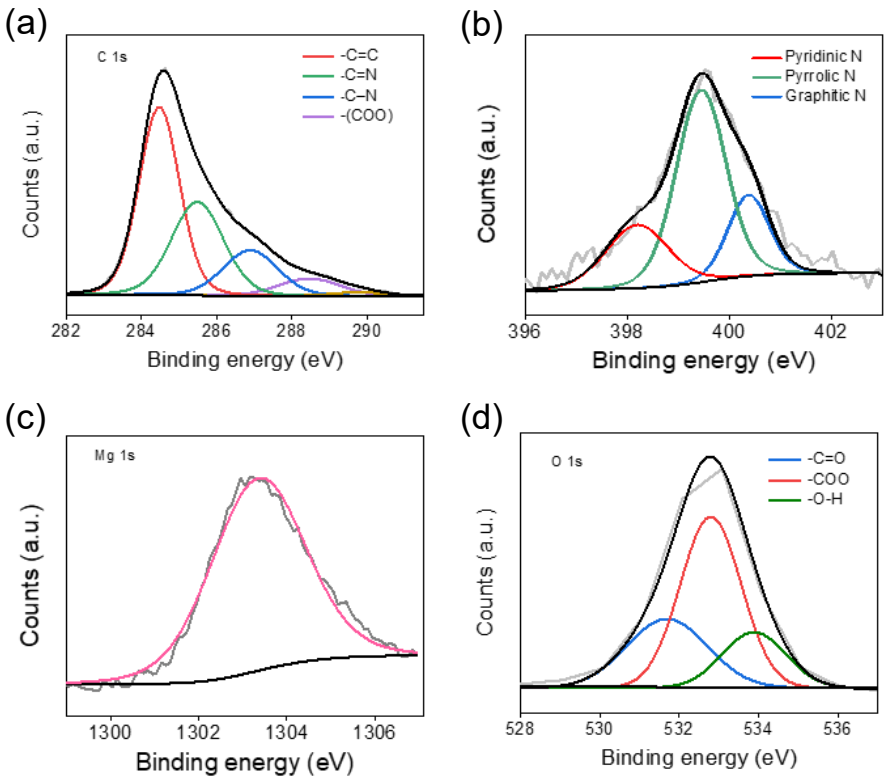

Figure. S7. (a) C 1s, (b) N 1s, (c) Mg 1s and (d) O 1s XPS spectra of MgNxC850.

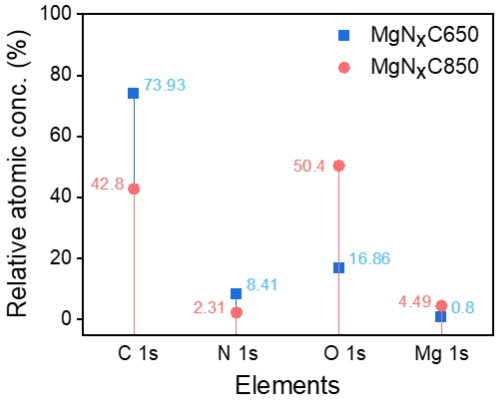

Figure. S8. Relative atomic concentrations (%) for MgNxC650 and MgNxC850 as respective elements.

7. FTIR studies of MgNxC650 and MgNxC850

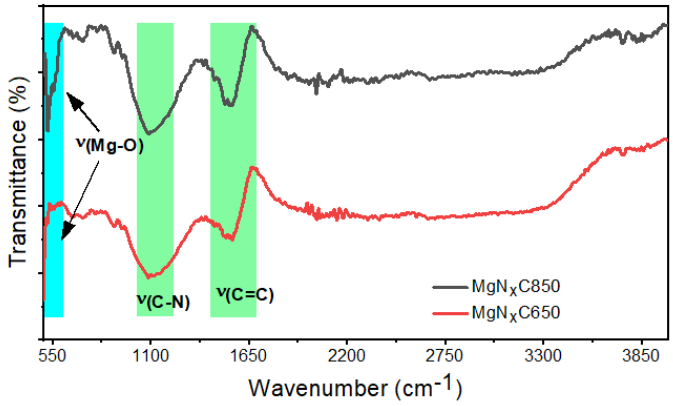

Figure. S9. FTIR spectra of MgNxC650 and MgNxC850. The peak at near 550 cm^{-1} corresponds to the stretching frequency of Mg-O bond.

8. Thermogravimetric analysis (TGA)

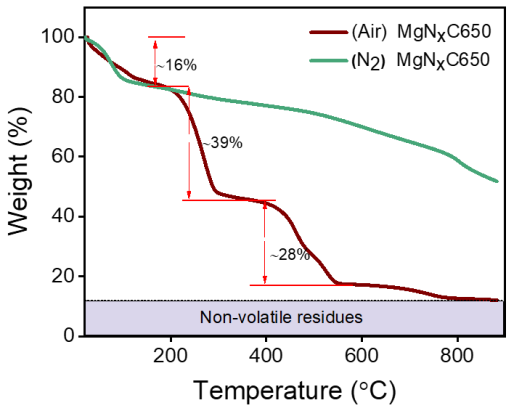

Figure. S10. Thermogravimetric analysis (TGA) performed in N_2 and air ambiance.

9. BET analysis

Table S3. Summary of BET analysis with different parameters

Catalysts	Single point Surface area (m^2/g)	Multi-point surface area (m^2/g)	Average Pore size (Radius) (Å)	Total pore volume (cc/g)
MgNxC550	671.9306	611.309	1.10974e+01	3.392e-01
MgNxC650	357.7384	369.440	1.09763e+01	2.028e-01
MgNxC750	293.8711	301.006	1.28879e+01	1.867e-01
MgNxC850	79.4145	83.754	1.42979e+01	5.988e-02

10. Electrochemical analysis

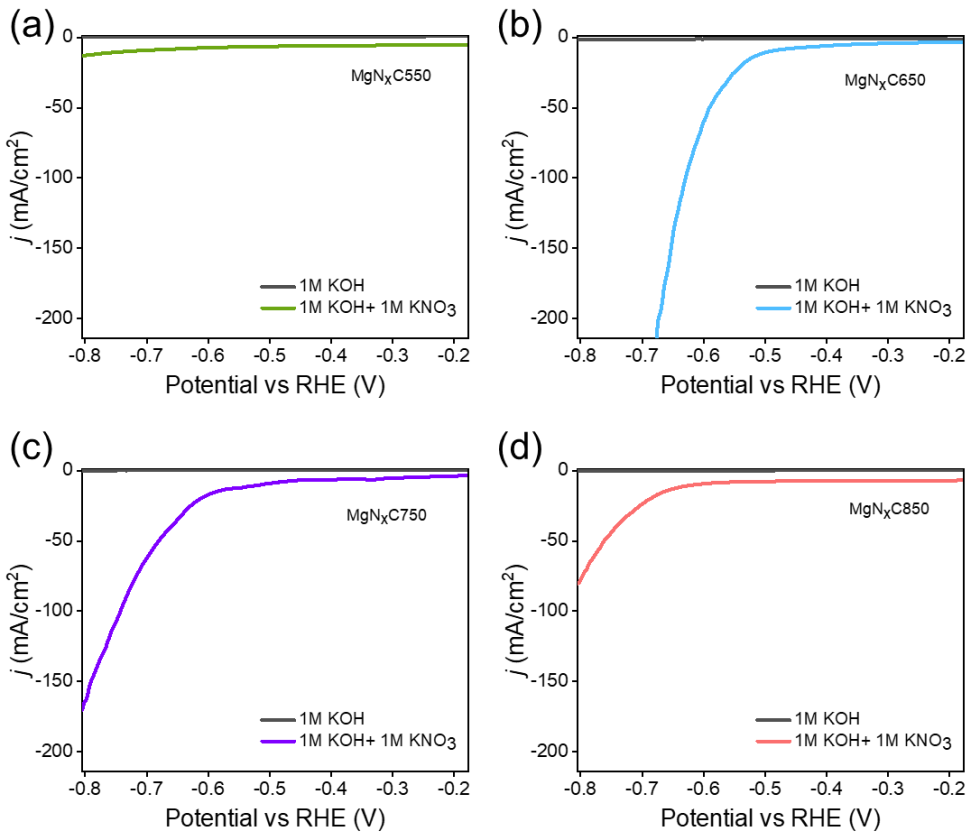

Figure. S11. Linear sweep voltammetry (LSV) measurements for MgNxC catalysts with and without nitrate source.

11. Concentration-dependent studies

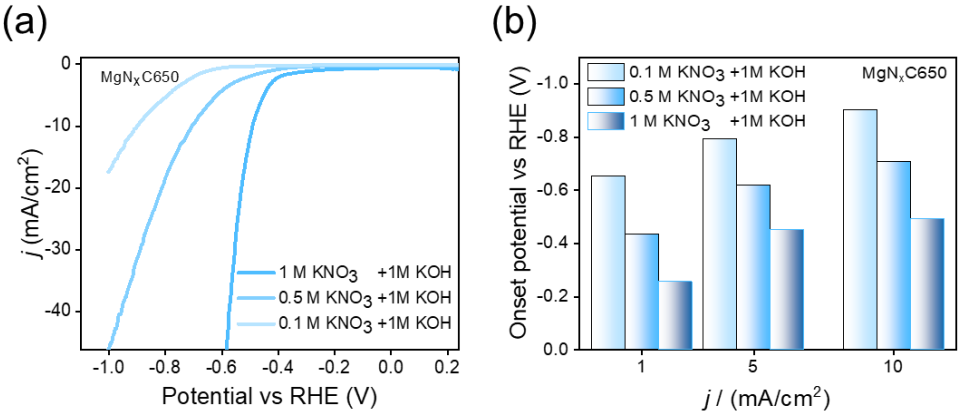

Figure. S12. (a) Different concentrations of nitrate source, and (b) Onset potential and overpotential.

12. Cyclic test studies

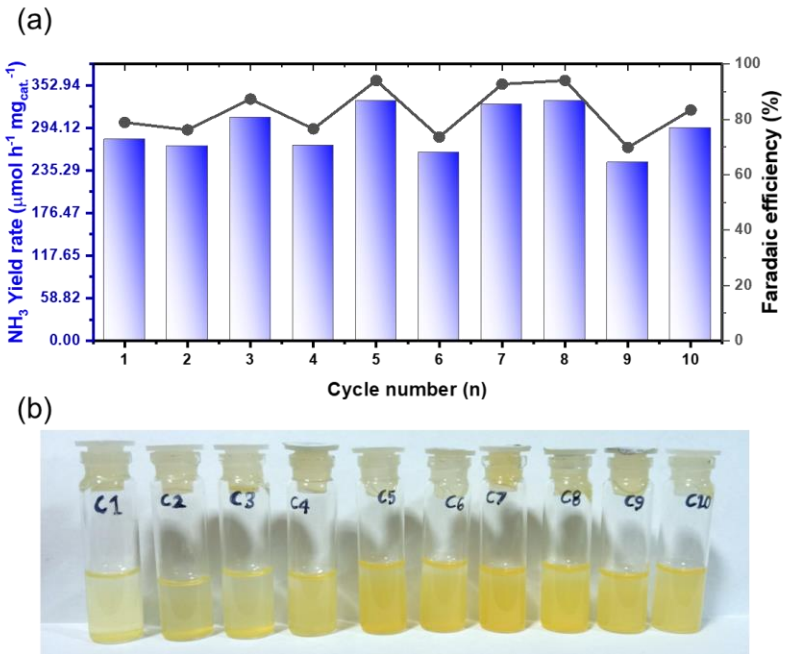

Figure. S13. Cyclic test performed for 30 minutes each for 5 h showing repeatability by MgNxC650 at -0.58 vs RHE (V).

13. Time-dependent studies

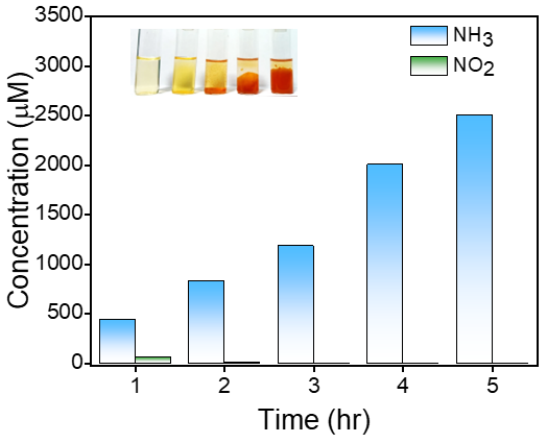

Figure. S14. Time-dependent studies of MgNxC650 at -0.58 vs RHE (V) toward ammonia production.

14. Quantification of the ions from the Cathodic compartment

We quantified the ion formed after the chronoamperometric test using the UV-Vis spectrophotometer (Hitachi U-2900 double-beam spectrophotometer) and NMR spectroscopy, and further quantified by the Ion-exchange chromatography using the calibration plots. Absorption spectra were analyzed according to the literature [36, 37].

15. Product analysis and efficiency calculations

15.1. UV- Visible spectroscopy

15.1.1. Nessler's method

All the experiments carried out for the ammonia with the best-optimized volumetric ratio of 5:15:3, where 500 µL Nessler's reagent (used as received), 1500 µL of 2M potassium hydroxide (prepared), and 300 µL calibration solutions of different concentrations of NH_4Cl taken for calibration respectively, Figure S15. To quantify the concentration of ammonia in the reaction product, 300 µL of the cathodic reaction product taken instead of NH_4Cl, keeping the same ratio as calibration.

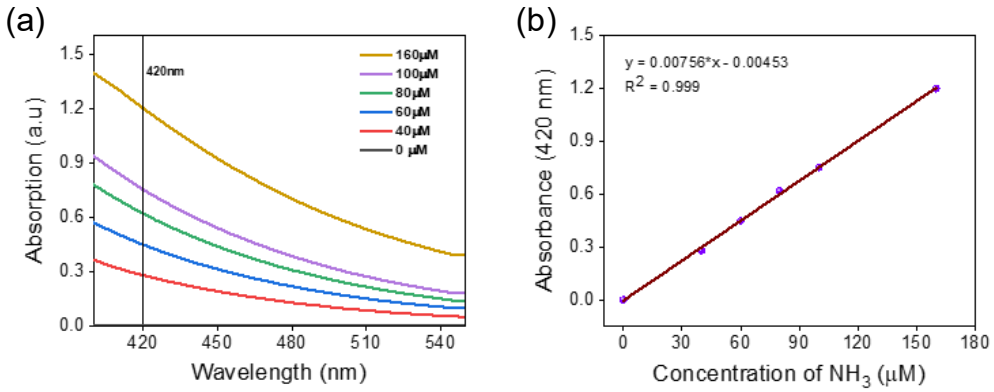

Figure. S15. (a) UV-Visible spectrum and (b) Calibration curve plot for estimation of NH_4^+ ion.

15.1.2. Griess's reagent test for NO_2^- anion

The nitrite ion indicator solution was prepared by dissolving 25 mg of "Modified Griess' reagent" in 5 mL of deionized (DI) water. The optimized volumetric ratio of 5:10:3, where 500 µL of Griess's reagent mixture with 300 µL of the sodium nitrite concentration solutions of 0, 2, 4, 6, 10, and 12 µM and 1000 µL of diluted phosphoric acid (H_3PO_4) was utilized with the optimized exposure time of 20 minutes. Similarly, for the nitrite concentration in the cathodic reaction product, reaction product of volume 300 µL taken instead of sodium nitrite concentration, keeping the ratio same. Finally, the calculations were done using the calibration plots shown in Figure S16.

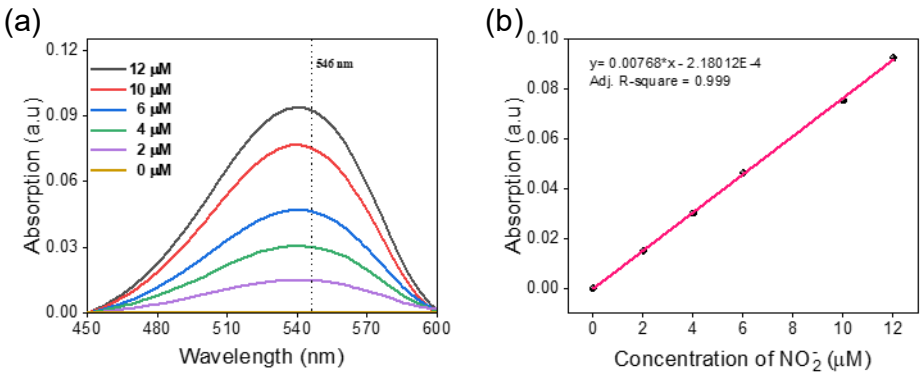

Figure. S16. (a) UV-Visible spectrum and (b) Calibration curve plot for the estimation of NO_2^-

15.2. NMR spectroscopy

^{1}H NMR employed to quantify our desired product by optimized the best scenario of solutions at pH 2-4, which are as 300 µL DMSO-*d6*, 10 µL of 0.079M of $C_4H_4O_4$, 350 µL of 1M H_2SO_4, and 0 to 180 µL of NH_4^+ for calibration plots shown in Figure S17. Similar protocols were followed for cathodic reaction products, by extracting 100 µL of the reaction product instead of NH_4^+ calibration solution, while keeping all parameters constant as calibration.

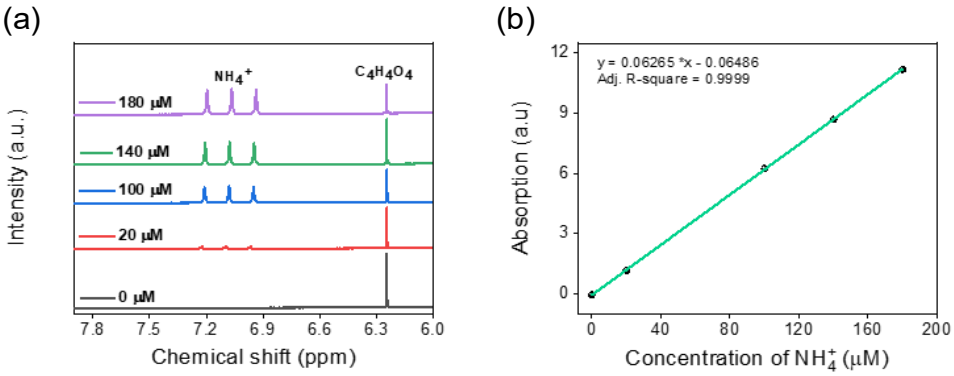

Figure. S17. (a) NMR response at different NH_4^+ concentrations and (b) Calibration curve plot for the estimation of NH_4^+ ion using NMR. spectroscopy.

15.3. Ion-exchange (IC) chromatography

In the context of our study, IC measurements were performed by recording the baseline curve of water and then aqueous solutions containing different concentrations of NH_4Cl salt as the source of ammonium cation (NH_4^+). We optimized and further quantified the ammonia in experimental cathodic reaction product solutions by sufficiently diluting to the solution medium having pH of around 11-12. The respective discussed plots for ammonium and nitrite ions are depicted in Figure S18 and S19.

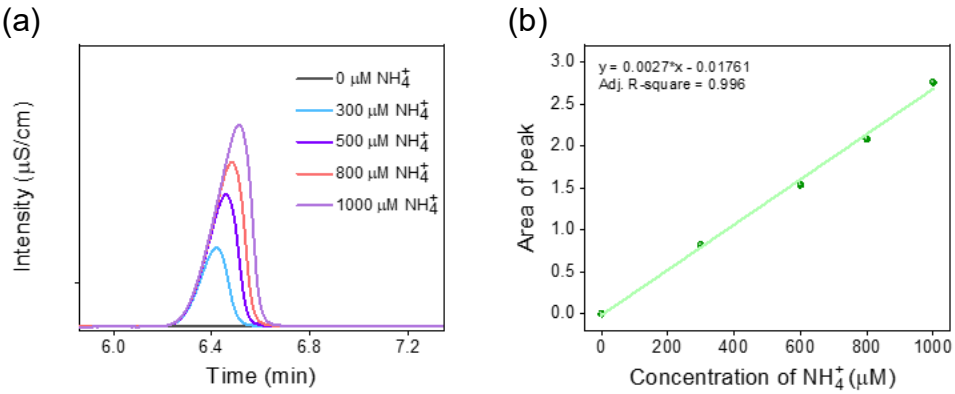

Figure. S18. (a) Ion-exchange chromatograms, and (b) Calibration curve plot for the estimation of NH_4^+ ion.

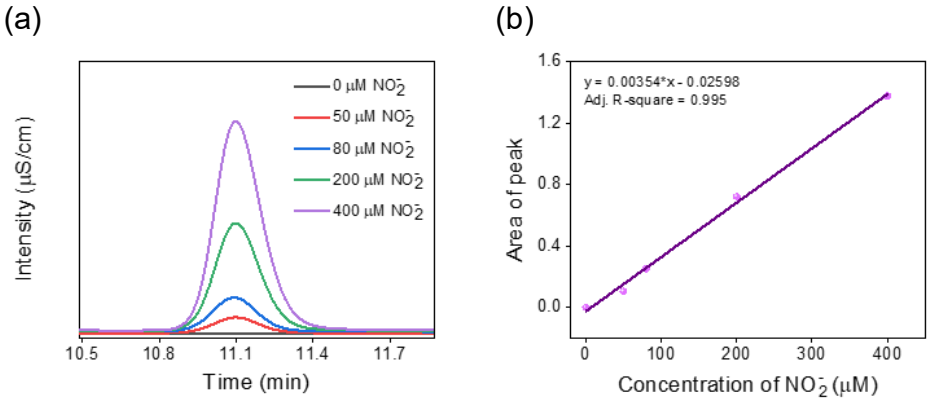

Figure. S19. (a) Ion-exchange chromatograms, and (b) Calibration curve plot for the estimation of NO_2^- ion.

16. Cyclic voltammetry (CV) and electrochemical double-layer capacitance (C_{dl}) determination

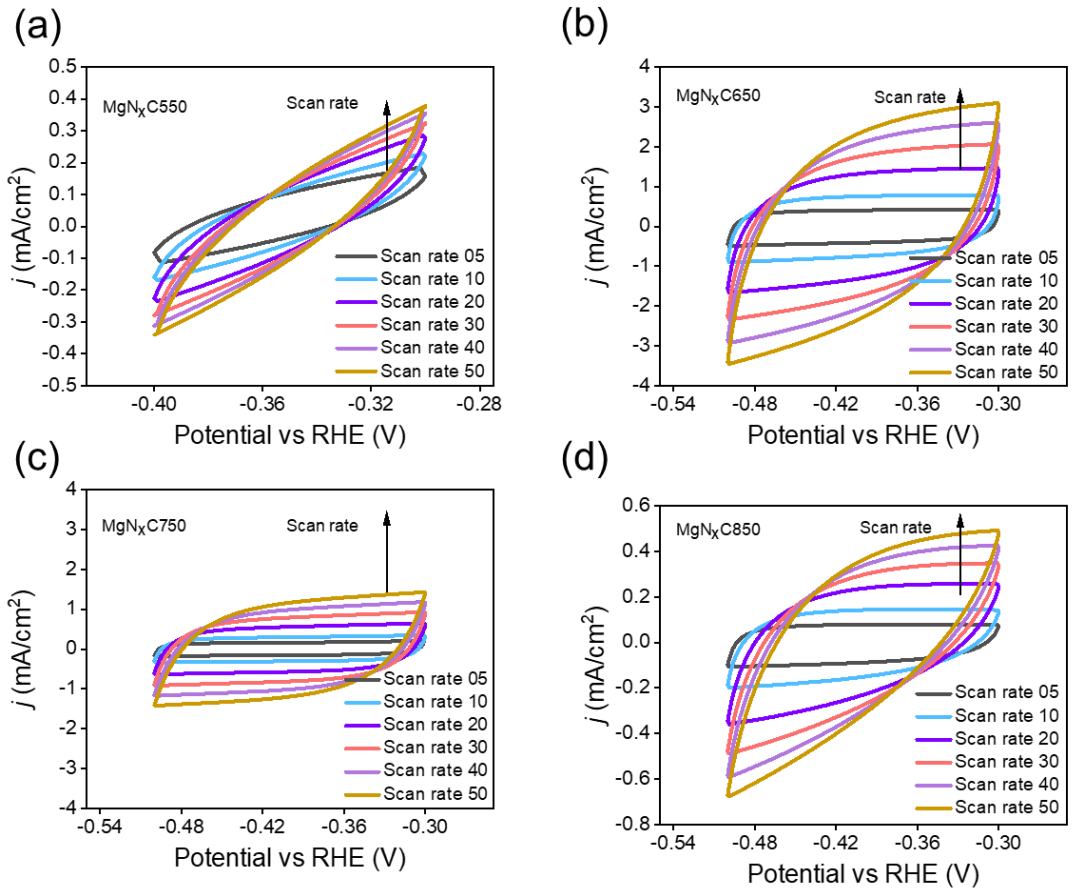

Figure. S20. Cyclic voltammetry curves of (a) MgNxC550, (b) MgNxC650, (c) MgNxC750, and (d) MgNxC850.

17. Mott-Schottky analysis

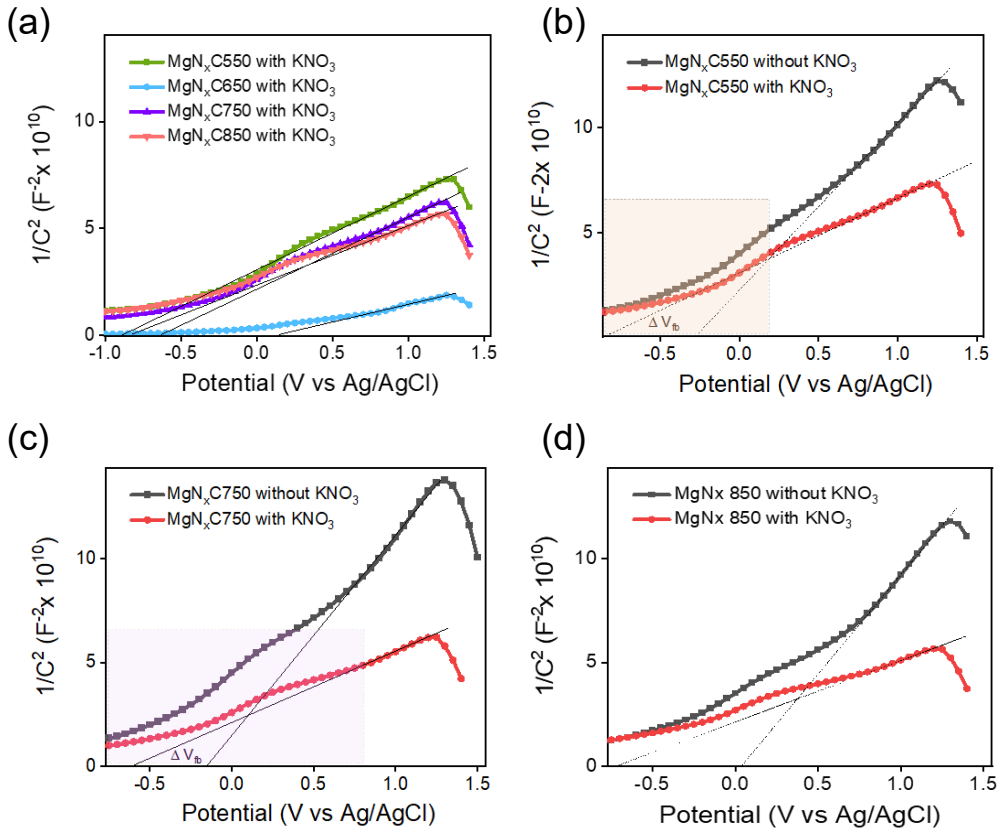

Figure. S21. (a) Mott-Schottky (M-S) plots of MgN_xC samples after introducing 1M KNO_3 in 1M KOH electrolyte medium. (b) Comparison of deviation in the M-S plot before and after the addition of KNO_3 on MgN_xC550, (c) MgN_xC750, and (d) MgNxC850.

18. Scherrer's equation for particle size calculation

We estimated the crystalline size of the nanoparticles for MgNxC850 from an x-ray diffraction peak using Scherrer's equation

$$D = \frac{k\lambda}{\beta \cos\theta}$$

where k, λ, β and θ are 0.9, 1.5406 Å, FWHM (full-width half maxima of well-identified peaks) in radians and theta (in radians)..

19. Computational Details

The formation energies of N-doped graphene structures in units of eV/N atom is defined as:

$$E_{formation} = \frac{E_{final} - n * E_{C(graphene)} - \frac{1}{2} m * E_{N_2(g)}}{m}$$

Where, $E_{formation}$ is the formation energy of the structure, E_{final} is the DFT calculated energy of the substrate, $E_{C(graphene)}$ and n, and $E_{N_2(g)}$ and m are the energies of per carbon atom in monolayer graphene and the number of carbon atoms and nitrogen gas molecule and the number of nitrogen atoms in the substrate, respectively. Further, the formation energy of Mg-doped SAC with various pyridinic atoms is calculated as

$$E_{SAC} = E_{final} - n * E_{C(graphene)} - \frac{1}{2} m * E_{N_2(g)} - E_{Mg/atom}$$

The computational hydrogen electrode (CHE) model, as proposed by Norskov. et.al [38], is used to calculate the adsorption energies of the intermediates. In this method, the chemical potential of a proton and electron pair in solution is defined as being the same as half the chemical potential of a gas phase H_2 molecule. The adsorption energy of NO_3^- was calculated using gaseous HNO_3 as a reference species.

$$E_{ads}(NO_3^*) = E_{NO_3^*} - E_{substrate} - E_{HNO_3(g)} + \Delta E_{correction}$$

where $E_{ads}(NO_3^*)$, $E_{NO_3^*}$ $E_{substrate}$, and $E_{HNO_3(g)}$ are the adsorption energy of NO_3, DFT calculated energy of adsorbed NO_3 intermediate and the gaseous HNO_3 molecule, respectively. In actual experiments, to account for the NO_3^-(aq) rather than HNO_3(g) a solvation correction, $\Delta E_{correction}$, of 0.392 eV accounting for HNO_3(g) → HNO_3(l) and HNO_3(l) → NO_3^-(aq) + H^+(aq) was applied to calculate the adsorption energy of $*NO_3$ [39, 40] .

The adsorption energy of different reaction intermediates involved in the reaction is calculated by the following expression,

$$E_{ads}(intermediate)^* = E_{intermediate}{}^* - E_{substrate} - E_{intermediate}$$

where $E_{ads}(intermediate)^*$ represents the adsorption energy of the intermediate and $E_{intermediate}{}^*$, $E_{substrate}$, and $E_{intermediate}$ are the DFT calculated energies of the adsorbed intermediate on the catalyst surface, tetracoordinated Mg-SAC substrate and the reference intermediate, respectively. The referencing

of the reaction intermediates involved is done as suggested by Vallejo et. al [41] and the list of reactions are given in Table S4.

Further, the adsorption energies are converted to Gibb's free energy of adsorption (ΔG_{ads}) by adding the zero-point energies and entropy contributions of the adsorbate, given by the following equation:

$$\Delta G_{ads} = E_{ads} + \Delta ZPE - T\Delta S$$

where ΔZPE is the difference between the zero-point energies of the adsorbate and the reference intermediates and ΔS is change in their entropies due to vibrational contribution and temperature (T) is taken as 298.15 K. The zero-point energy (ZPE) correction and the entropy of the adsorbate as well as the reference species at 298.15 K were calculated using the VASPkit package[42].

For adsorbate on the catalyst, all 3N modes are considered as vibrational modes under harmonic oscillator approximation. Visualization of the structures was done using the VESTA package [10, 43]. Bader charge scheme was utilised to study the degree of charge distribution in the substrate and adsorbate [44]. The ZPE and entropy corrections of the reference gaseous molecules HNO_3(g) and H_2(g) is provided in Table S5. The limiting potential (U_L) for the reaction is calculated by taking negative of the maximum free energy difference (ΔG_{max}) between two successive steps in the free energy diagram.

$$\Delta G_{max} = max\{\Delta G_1, \Delta G_2, \Delta G_3 \dots\}$$

$$U_L = -\frac{\Delta G_{max}}{e}$$

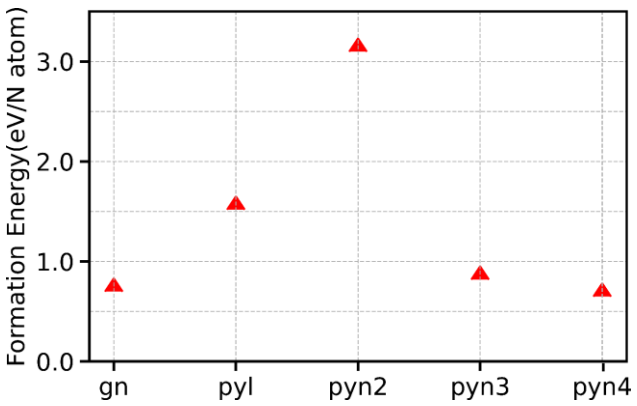

Figure. S22. Formation energies of N-doped structures showing g-N, pyridinic-3 (pyn3) and pyridinic-4 (pyn4) are relatively more stable than pyrrolic and pyridinic-2 (pyn2).

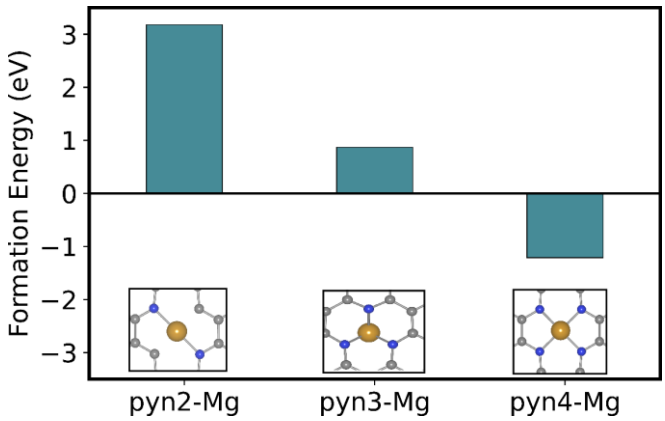

Figure. S23. Formation energy of Mg-SAC with Mg coordinated to two, three and four N atoms. Tetracoordinated Mg atoms are most stable forming the Mg-SAC substrate.

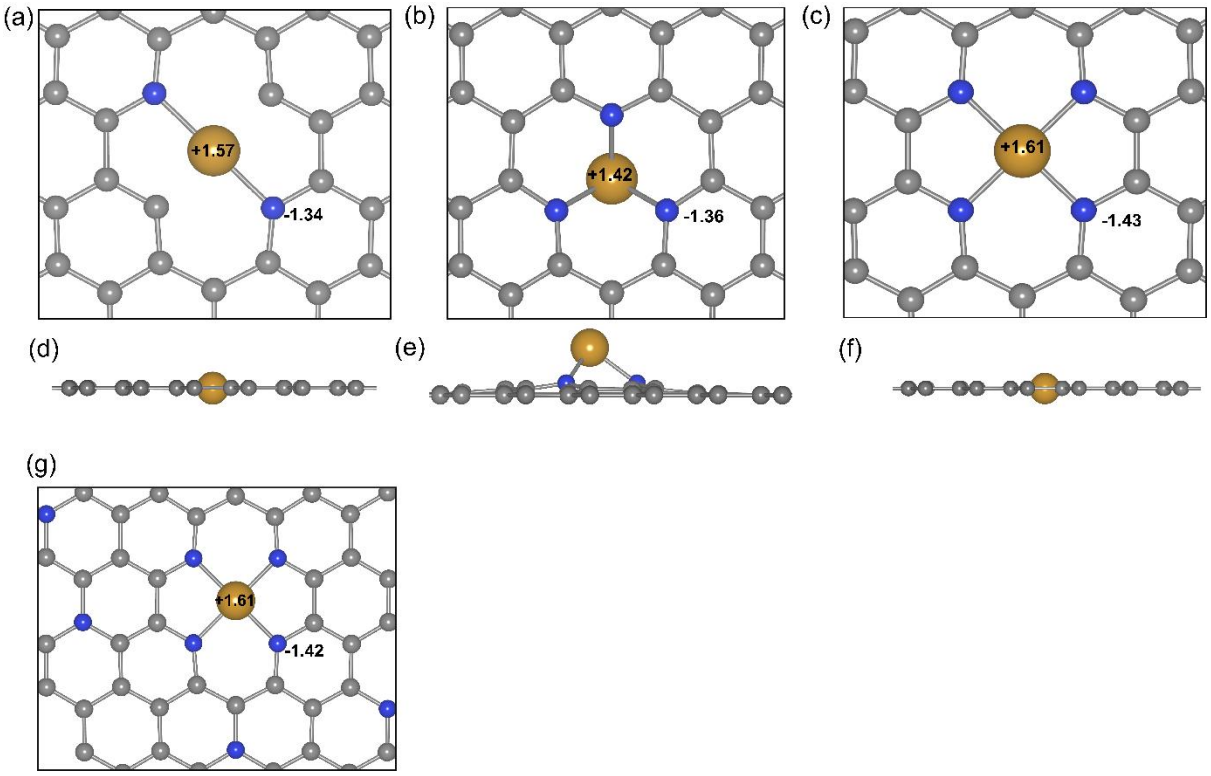

Figure. S24. Bader charge distributions of Mg and N atoms in the substrate. In plane Mg atoms in (a) pyn2 and (c)pyn4 show better charge transfer between Mg and N atoms. For (b) pyn3, Mg atom moves out of the plane, and (g) the final substrate structure.

NRA2: *NO3 → *HNO3 → *NO2 → *HNO2 → *NO → *NOH→ *NHOH → *NH → *NH2 → *NH3

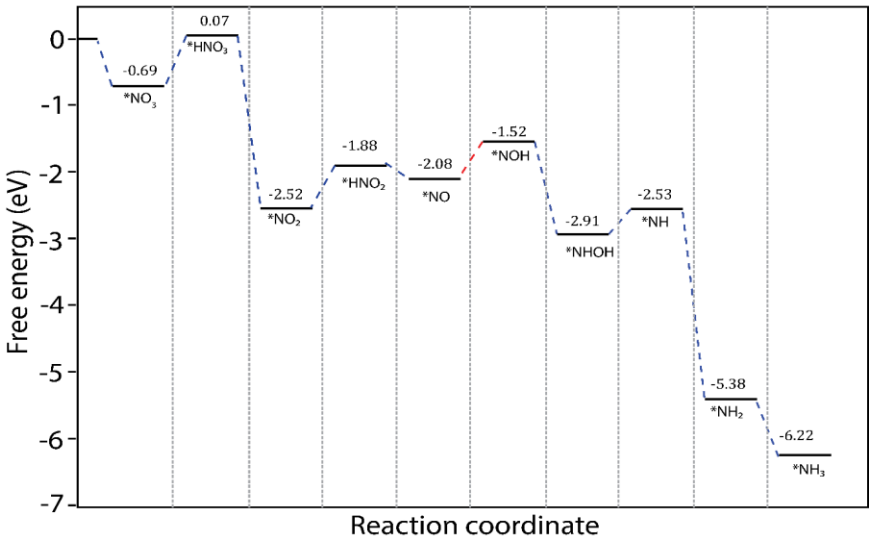

Figure. S25. Calculated free energy diagram for the NRA2 where, on *NO, hydrogenation takes place on oxygen atom. This step is thermodynamically uphill.

NRA3: *NO3 → *HNO3 → *NO2 → *HNO2 → *ON → *ONH/*HON→ *NHOH → *ONH2/NH2OH(g) → *O + NH3(g)

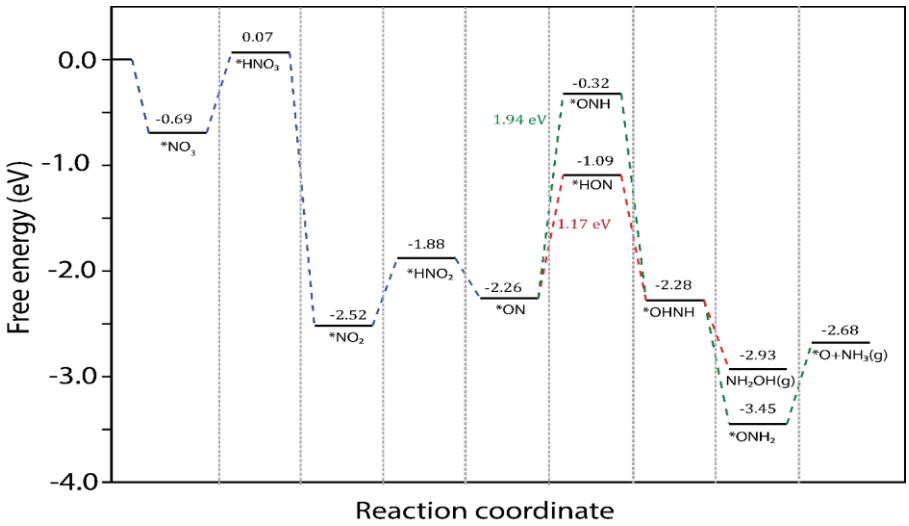

Figure. S26. Calculated free energy diagram for the NRA3 where, on *ON, hydrogenation takes place on O and N, leading to *HON and *ONH with thermodynamic potential barriers of 1.17 and 1.94 eV respectively.

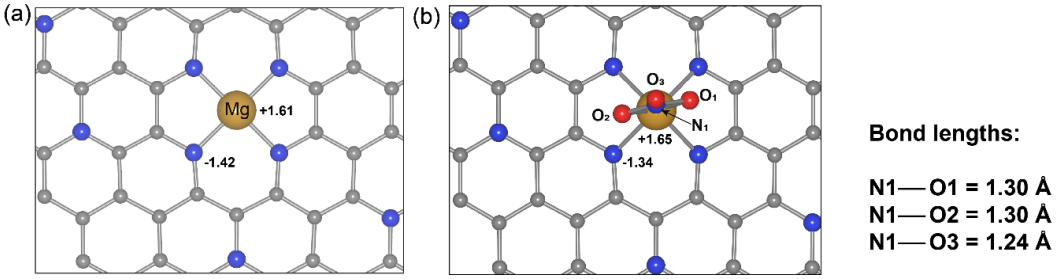

Figure. S27. Charge distribution on the substrate (a) before and (b) after adsorption of *NO_3 and the elongation of N-O bonds after *NO_3 adsorption.

Table S4: List of reactions involved for calculation of adsorption energies of each intermediate, considering HNO_3 and H_2 in gas phase as reference species, as suggested by Calle- Vallejo et. al [41] [18].

$HNO_3 + * \rightarrow *NO_3 + 1/2H_2$
$HNO_3 + * \rightarrow *HNO_3$
$HNO_3 + H_2 + * \rightarrow *HNO_2 + H_2O$
$HNO_3 + 1/2H_2 + * \rightarrow *NO_2 + H_2O$
$HNO_3 + 3/2H_2 + * \rightarrow *NO + H_2O$
$HNO_3 + 3/2H_2 + * \rightarrow *ON + H_2O$
$HNO_3 + 2H_2 + * \rightarrow *HNO + 2H_2O$
$HNO_3 + 2H_2 + * \rightarrow *NOH + 2H_2O$
$HNO_3 + 2H_2 + * \rightarrow *ONH + 2H_2O$
$HNO_3 + 2H_2 + * \rightarrow *HON + 2H_2O$
$HNO_3 + 5/2H_2 + * \rightarrow *NHOH + 2H_2O$
$HNO_3 + 3H_2 + * \rightarrow *NH_2OH + 2H_2O$
$HNO_3 + 5/2H_2 + * \rightarrow *ONH_2 + 2H_2O$
$H_2O + * \rightarrow O* + H_2$
$HNO_3 + 5/2H_2 + * \rightarrow N* + 3H_2O$
$HNO_3 + 3H_2 + * \rightarrow *NH + 3H_2O$
$HNO_3 + 7/2H_2 + * \rightarrow *NH_2 + 3H_2O$

$HNO_3 + 4H_2 + * \rightarrow NH_3* + 3H_2O$
$HNO_3 + 3/2H_2 \rightarrow NO(g) + 2H_2O$
$HNO_3 + 1/2H_2 \rightarrow NO_2(g) + H_2O$

Table S5: Total energy, zero-point energy (ZPE) and entropy corrections (TΔS) for the reference gaseous molecules.

Reference Molecule	Total Energy (Eref) (eV)	ZPE (eV)	TΔS (eV)
HNO_3	-28.62	0.69	0.68
H_2	-6.69	0.27	0.41

20. Experimental Procedures

20.1. Selection of precursors and their respective roles in MgNxC catalyst synthesis

The detailed synthetic procedures and role of respective precursors utilized in our work are described in the following sections:

1. Chlorophyll extract: We have taken the opportunity to utilize the natural green leaves of *Spinacia oleracea* with higher enrich in Magnesium metal as the source.
2. Coffee filtrate: We have taken 70% caffeine + 30% chicory-containing coffee powder purchased from Nestlé, India. The reason behind the filtration is to take as small particles as possible for grinding and mix well with other chemical precursors. The interest in using filter coffee lies in the following reasons:
    i. Caffeine is a source of Carbon and Nitrogen[45], and could be used to provide multiple coordination sites for magnesium metal ions to interact and increase the probability of reaction [46, 47]
    ii. It works as a supporting precursor and helps to create and modify the graphene sheet[47].
    iii. Moreover, it is highly abundant in nature, non-toxic, highly cost-effective, and environmentally friendly.
3. Ammonium chloride (NH_4Cl): Ammonium chloride prevents the quenching of any organo-magnesium compound and avoids any side reaction with magnesium ions. Being acidic salt, it makes the aqueous precursor mixture a bit acidic that provides caffeine an acidic medium, thereby increasing the solubility of the primary precursor mixture of chlorophyll extracts, filtered coffee powder etc.
4. A 2 mg of Ammonium molybdate ($(NH_4)_6Mo_7O_{24}.4H_2O$) is used for catalyzing the reaction. It may be noted that no trace of Mo was found in our sample.

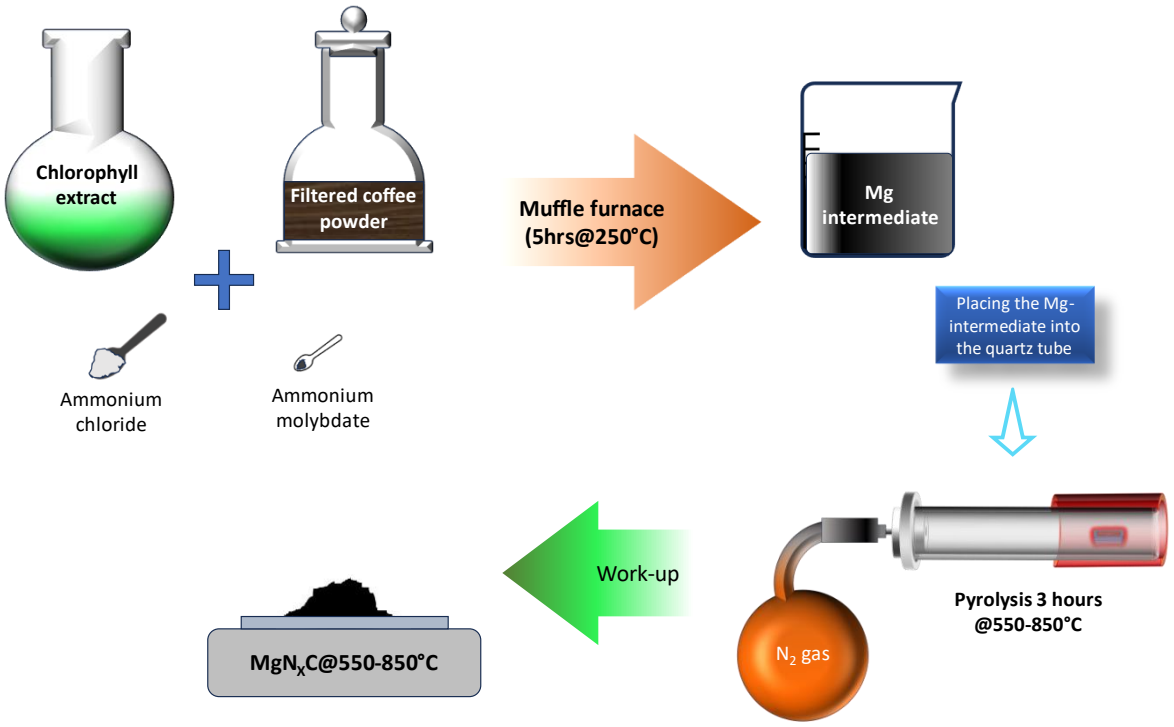

Figure. S28. Schematic diagram of Synthetic procedure of MgNxC catalyst at different temperatures.

20.2. Extraction of chlorophyll

Step 1: Green leaves of spinach are collected. The leaves were gently scrubbed and washed well with rinse under running water. After well cleaned, leaves are wiped with cotton and dried for a few minutes in hot oven at ~40°C.

Step 2: Spinach leaves are crushed into small pieces to get a faster chlorophyll extraction rate. A 250 ml beaker was filled with crushed leaves and 100 ml of ethanol as shown in the figure S28. It is mixed with a

Spinach leaves | Leaves + Ethanol | Chlorophyll extract

Figure. S29. Schematic diagram for chlorophyll extraction from spinach leaves at temperature of 80-85°C

glass rod and left for 10 mins at 85°C. After 10 minutes, the greenish liquid was collected in separate conical flasks, filled with 100 ml ethanol, stirred again, and repeated until clear liquid appeared. After a while, about 250 ml of liquid solution was collected and again concentrated by putting it on a hot plate and stirring at 85°C overnight.

20.3. Analysis of Chlorophyll extract

We analyzed the chlorophyll extract by obtaining the UV-Vis spectra using the Hitachi U-2900 double-beam spectrophotometer shown in Figure S30.

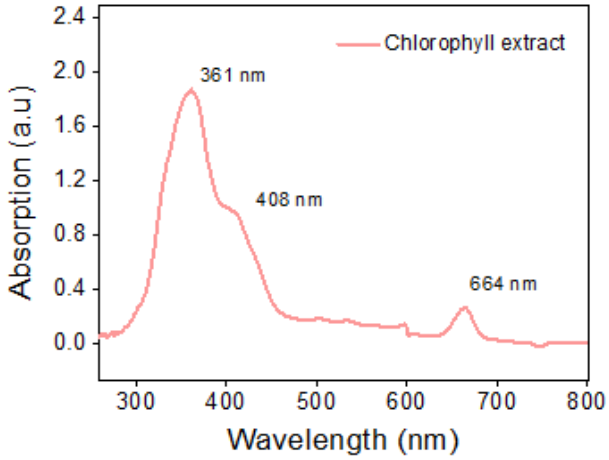

Figure. S30. UV-Visible spectra of extracted chlorophyll solution from Spinach leaves.

20.4. Physical filtration and selection of coffee powder

We have collected the coffee powder of Nestlé coffee, having Coffee 70% and Chicory 30% from the market. In the process of further filtering the coffee powder from its big particles, we used a flour sieve and ensured the uniformity of small coffee particles and named as filtered coffee powder. As filtered coffee

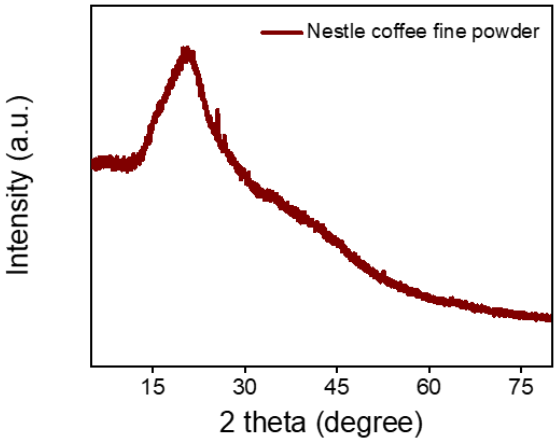

Figure. S31. X-Ray diffraction pattern of coffee powder after sieve filtration.

powder were sensitive to moisture, we put it in the hot oven for preservation. For, the sake of characterization, X-ray diffraction patterns were collected and shown in Figure S31.

20.5. Preparation of precursors

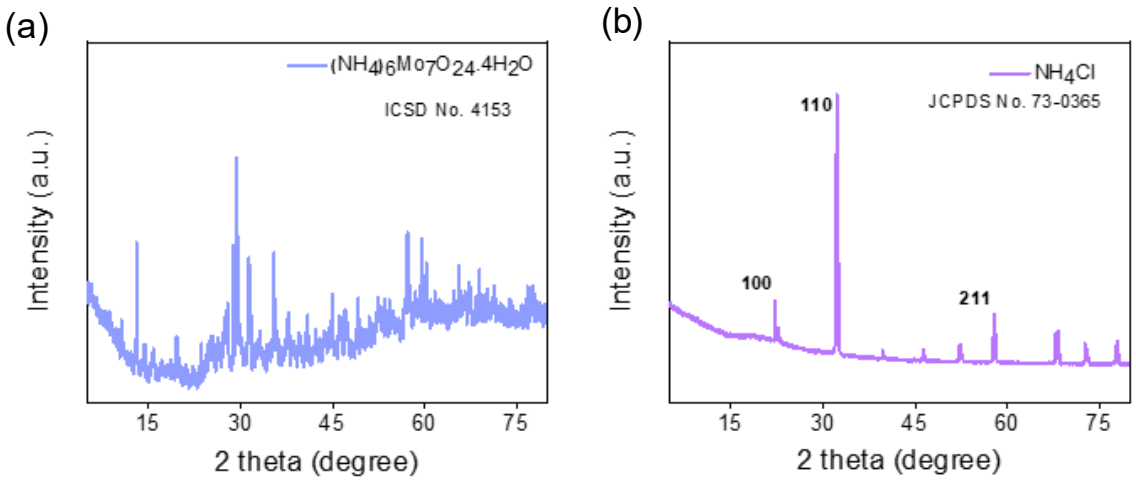

Figure. S32. X-Ray diffraction pattern (a) ammonium molybdate and (b) ammonium chloride.

Chlorophyll extract (25 ml), filtered coffee powder (20 g), a small amount of ammonium chloride (0.15 g), and a very less than a pinch of ammonium molybdate (0.002 g) are added and put in a muffle furnace at a slow temperature ramping rate of 10°C/min at 250°C for a dwelling time of 5 h to remove the moisture and facilitate the ease of homogenous mixture and graphene synthesis. After we collected the faded blackish-fluffy materials and termed them as Mg-intermediate.

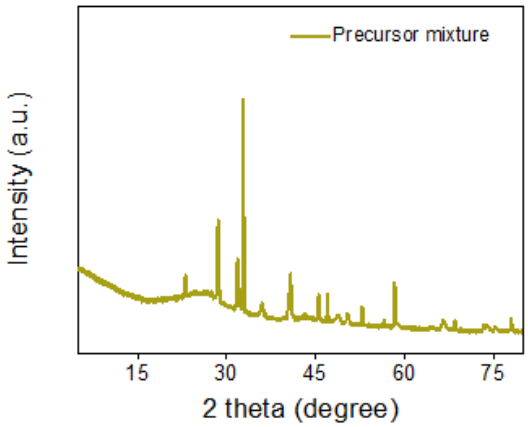

Figure. S33. X-Ray diffraction pattern of mixture of precursors (Chlorophyll solution + coffee powder+ ammonium chloride and ammonium molybdate.

20.6. Mg-intermediate Processing:

Mg-intermediate is washed with water and acetone to remove any ionic or elemental impurities and named Mg-intermediate-washed. X-ray diffraction patterns were collected for both Mg-intermediate and after washing the Mg-intermediate, Figure S34. Then it was subjected to pyrolysis at different temperatures.

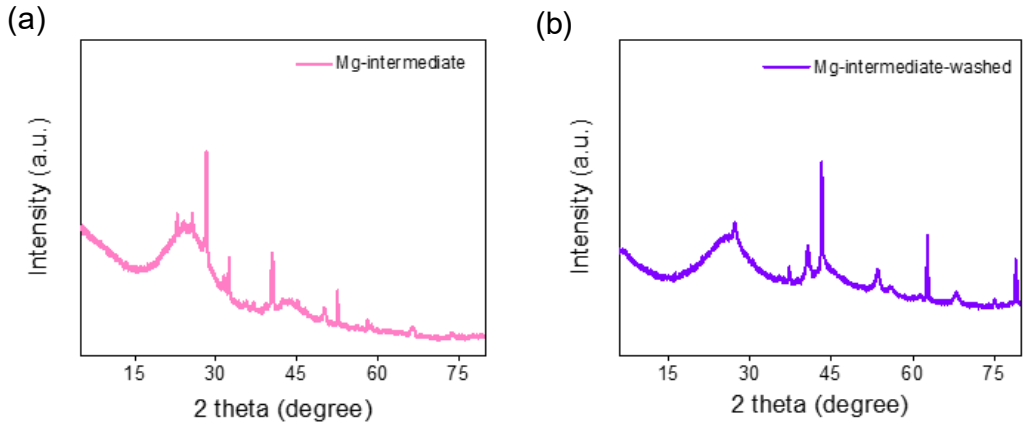

Figure. S34. X-Ray diffraction (a) product after muffle furnace (Mg-intermediate) and the (b) Mg-intermediate after washing

20.7. Pyrolysis of Mg-intermediate

About 0.5 g of Mg-intermediate is filled in a Borosil quartz tube (one-sided end) of length 22.4 inches and 0.4 in diameter and is closed with an N_2 environment by a Nitrogen balloon. Mg-intermediate was pyrolyzed with a ramping rate of 10°C/min at different temperatures i.e., 550, 650, 750 and 850°C for 3 h and labeled as MgNxC550, MgNxC650, MgNxC750, and MgNxC850, respectively.

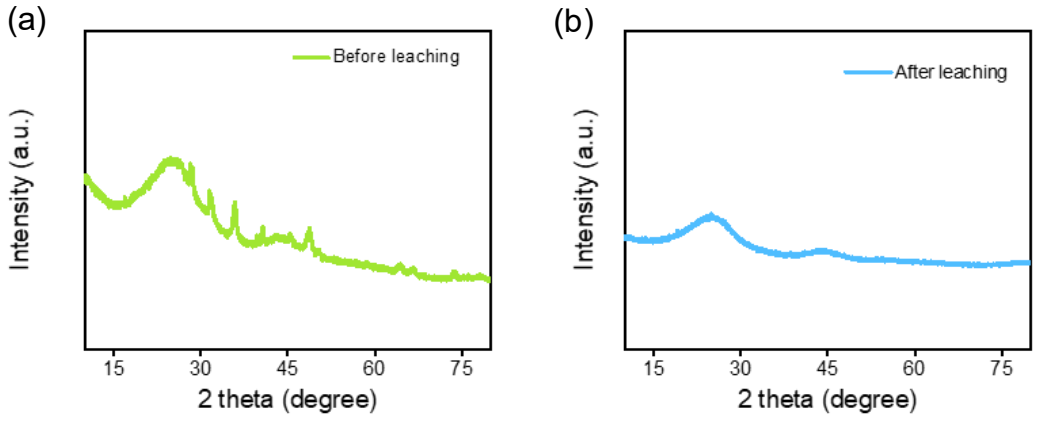

Figure. S35. X-ray diffraction pattern of a product after pyrolysis (a) before leaching (MgNxC650) and (b) after leaching (final product (MgNxC650) catalyst).

20.8. Catalysts chemical compositional analysis

We employed scanning electron microscopy coupled energy-dispersive X-ray spectroscopy (SEM-EDS). Following are the plots depicting the SEM-EDS analysis on final product (MgNxC650) at different regions. There is no signature of any other elemental impurities, viz., Molybdenum (Mo), or chloride ion. The reason for this is the washing off the sample with polar solvents like deionized water after muffle furnace treatment which eliminates the amount of any ionic or elemental impurities.

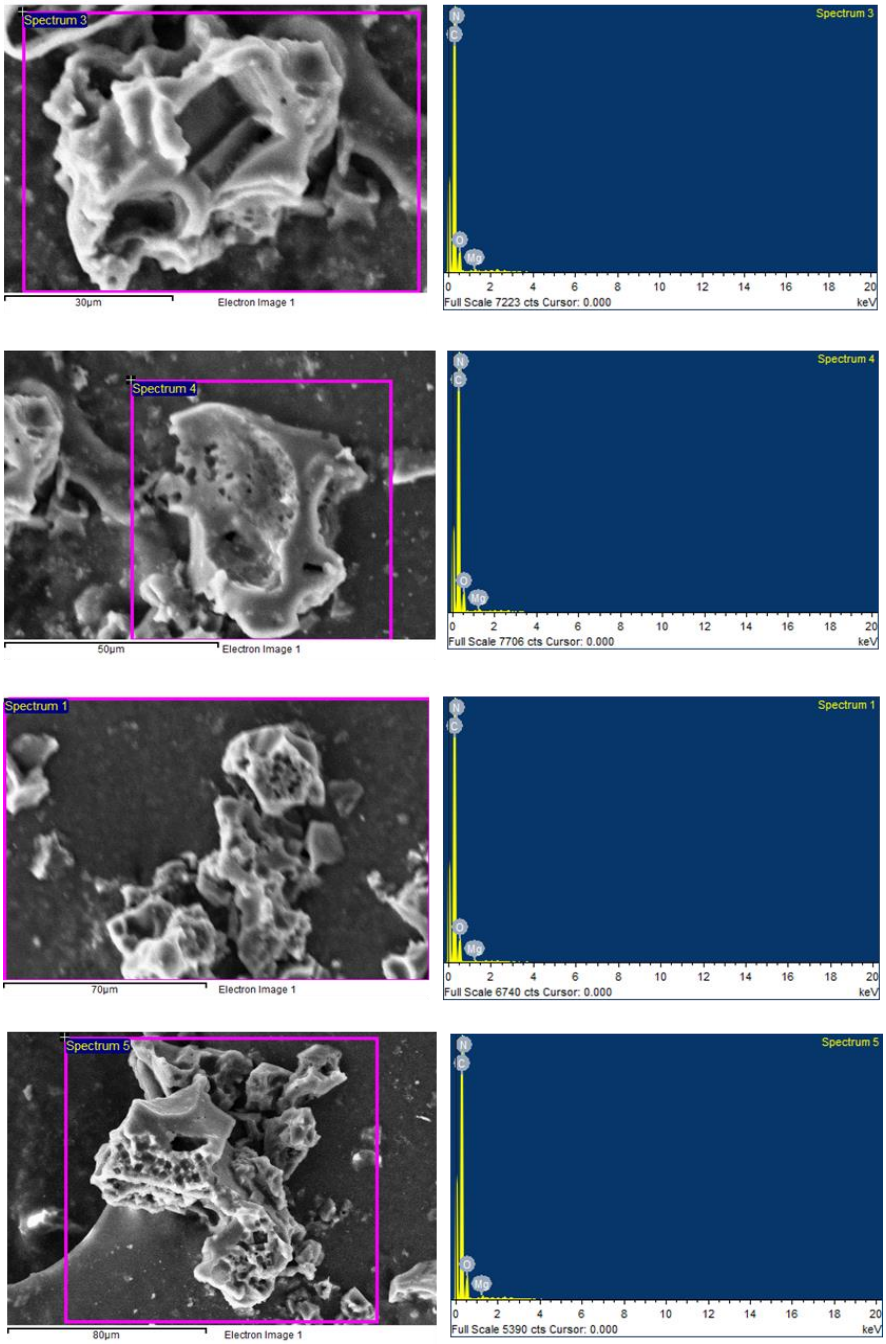

Figure. S36. SEM-EDS elemental spectra of final product (MgNxC650 catalyst) at different regions over a wide X-ray energy (keV) window.

21. Electrochemical measurements

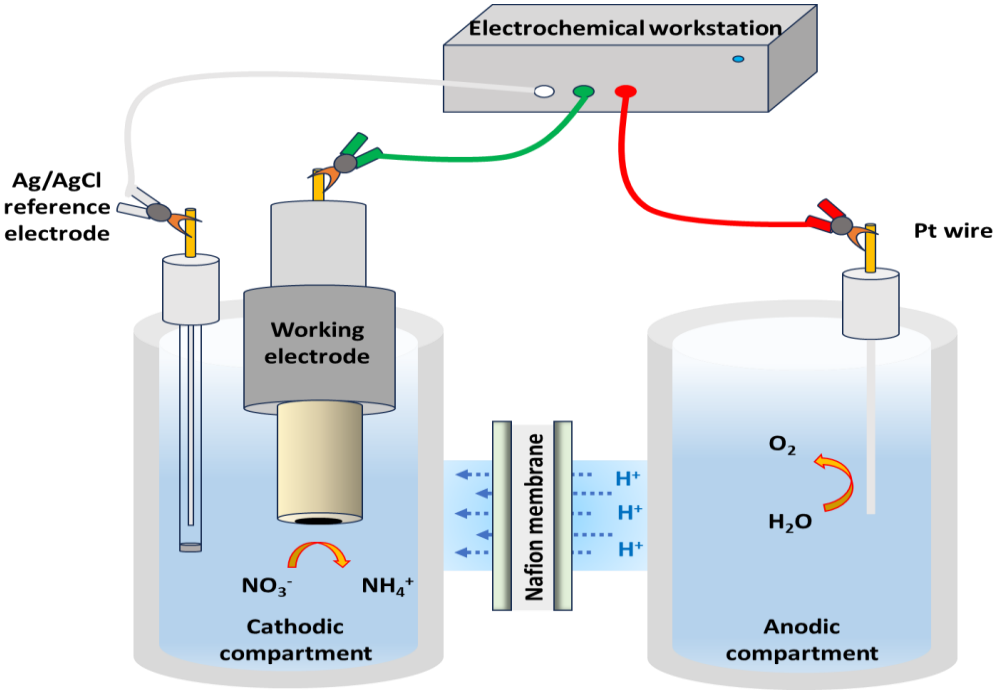

Figure. S37. Schematic diagram for electrochemical working setup.

References

1. Guo, S., et al., *A single-atomic noble metal enclosed defective MOF via cryogenic UV photoreduction for CO oxidation with ultrahigh efficiency and stability.* ACS applied materials & interfaces, 2020. **12**(23): p. 26068-26075.
2. Wang, H., et al., *Quasi Pd1Ni single-atom surface alloy catalyst enables hydrogenation of nitriles to secondary amines.* Nature communications, 2019. **10**(1): p. 4998.
3. Lin, J., et al., *Remarkable performance of Ir1/FeO x single-atom catalyst in water gas shift reaction.* Journal of the American Chemical Society, 2013. **135**(41): p. 15314-15317.
4. Qiao, B., et al., *Highly efficient catalysis of preferential oxidation of CO in H2-rich stream by gold single-atom catalysts.* ACS catalysis, 2015. **5**(11): p. 6249-6254.
5. Gu, X.-K., et al., *Supported single Pt1/Au1 atoms for methanol steam reforming.* Acs Catalysis, 2014. **4**(11): p. 3886-3890.
6. Kim, J., et al., *Highly durable platinum single-atom alloy catalyst for electrochemical reactions.* Advanced Energy Materials, 2018. **8**(1): p. 1701476.
7. Aich, P., et al., *Single-atom alloy Pd–Ag catalyst for selective hydrogenation of acrolein.* The Journal of Physical Chemistry C, 2015. **119**(32): p. 18140-18148.
8. Lucci, F.R., et al., *Selective hydrogenation of 1,3-butadiene on platinum–copper alloys at the single-atom limit.* Nature Communications, 2015. **6**(1): p. 8550.
9. Marcinkowski, M.D., et al., *Pt/Cu single-atom alloys as coke-resistant catalysts for efficient C–H activation.* Nature chemistry, 2018. **10**(3): p. 325-332.
10. Shan, J., et al., *NiCu single atom alloys catalyze the CH bond activation in the selective non-oxidative ethanol dehydrogenation reaction.* Applied Catalysis B: Environmental, 2018. **226**: p. 534-543.
11. Najafishirtari, S., et al., *The effect of Au domain size on the CO oxidation catalytic activity of colloidal Au–FeOx dumbbell-like heterodimers.* Journal of catalysis, 2016. **338**: p. 115-123.
12. Gan, T., et al., *Facile synthesis of kilogram-scale Co-alloyed Pt single-atom catalysts via ball milling for hydrodeoxygenation of 5-hydroxymethylfurfural.* ACS sustainable chemistry & engineering, 2020. **8**(23): p. 8692-8699.
13. Gan, T., et al., *Unveiling the kilogram-scale gold single-atom catalysts via ball milling for preferential oxidation of CO in excess hydrogen.* Chemical Engineering Journal, 2020. **389**: p. 124490.
14. Yu, L.-Q., et al., *Universal method to fabricate transition metal single-atom-anchored carbon with excellent oxygen reduction reaction activity.* ACS Applied Materials & Interfaces, 2021. **13**(11): p. 13534-13540.
15. Zhao, C., et al., *Ionic exchange of metal–organic frameworks to access single nickel sites for efficient electroreduction of CO2.* Journal of the American Chemical Society, 2017. **139**(24): p. 8078-8081.
16. Zhang, L., et al., *Efficient and durable Au alloyed Pd single-atom catalyst for the Ullmann reaction of aryl chlorides in water.* ACS Catalysis, 2014. **4**(5): p. 1546-1553.
17. Yin, P., et al., *Single cobalt atoms with precise N-coordination as superior oxygen reduction reaction catalysts.* Angewandte Chemie, 2016. **128**(36): p. 10958-10963.
18. Liu, S., et al., *Turning main-group element magnesium into a highly active electrocatalyst for oxygen reduction reaction.* Nature communications, 2020. **11**(1): p. 938.
19. Bisen, O.Y. and K.K. Nanda, *Alkaline earth metal based single atom catalyst for the highly durable oxygen reduction reaction.* Applied Materials Today, 2020. **21**: p. 100846.

20. Shao, X.-B., et al., *Magnesium single-atom catalysts with superbasicity.* Science China Chemistry, 2023. **66**(6): p. 1737-1743.
21. McEnaney, J.M., et al., *Electrolyte engineering for efficient electrochemical nitrate reduction to ammonia on a titanium electrode.* ACS sustainable chemistry & engineering, 2020. **8**(7): p. 2672-2681.
22. Jia, R., et al., *Boosting selective nitrate electroreduction to ammonium by constructing oxygen vacancies in TiO2.* Acs Catalysis, 2020. **10**(6): p. 3533-3540.
23. Wang, Y., et al., *Enhanced nitrate-to-ammonia activity on copper–nickel alloys via tuning of intermediate adsorption.* Journal of the American Chemical Society, 2020. **142**(12): p. 5702-5708.
24. Li, J., et al., *Efficient ammonia electrosynthesis from nitrate on strained ruthenium nanoclusters.* Journal of the american chemical society, 2020. **142**(15): p. 7036-7046.
25. Lu, C., et al., *Electroreduction of nitrate to ammonia in alkaline solutions using hydrogen storage alloy cathodes.* Electrochimica acta, 1999. **44**(13): p. 2193-2197.
26. Wang, Y., et al., *Unveiling the activity origin of a copper-based electrocatalyst for selective nitrate reduction to ammonia.* Angewandte chemie international edition, 2020. **59**(13): p. 5350-5354.
27. Wu, Z.-Y., et al., *Electrochemical ammonia synthesis via nitrate reduction on Fe single atom catalyst.* Nature communications, 2021. **12**(1): p. 2870.
28. Wang, Y., et al., *Self-template synthesis of hierarchically structured Co3O4@ NiO bifunctional electrodes for selective nitrate reduction and tetrahydroisoquinolines semi-dehydrogenation.* Sci. China Mater, 2020. **63**(12): p. 2530-2538.
29. Han, Y., et al., *Facet-controlled palladium nanocrystalline for enhanced nitrate reduction towards ammonia.* Journal of Colloid and Interface Science, 2021. **600**: p. 620-628.
30. Cai, J., et al., *Electrocatalytic nitrate-to-ammonia conversion with~ 100% Faradaic efficiency via single-atom alloying.* Applied Catalysis B: Environmental, 2022. **316**: p. 121683.
31. Choi, J., et al., *Electroreduction of nitrates, nitrites, and gaseous nitrogen oxides: a potential source of ammonia in dinitrogen reduction studies.* ACS Energy Letters, 2020. **5**(6): p. 2095-2097.
32. Liu, H., et al., *Efficient electrochemical nitrate reduction to ammonia with copper-supported rhodium cluster and single-atom catalysts.* Angewandte Chemie International Edition, 2022. **61**(23): p. e202202556.
33. Mi, L., et al., *Achieving synchronization of electrochemical production of ammonia from nitrate and ammonia capture by constructing a "two-in-one" flow cell electrolyzer.* Advanced Energy Materials, 2022. **12**(44): p. 2202247.
34. Zhang, X., et al., *Cu clusters/TiO 2− x with abundant oxygen vacancies for enhanced electrocatalytic nitrate reduction to ammonia.* Journal of Materials Chemistry A, 2022. **10**(12): p. 6448-6453.
35. Chen, Q., et al., *CoO nanoparticle decorated N-doped carbon nanotubes: a high-efficiency catalyst for nitrate reduction to ammonia.* Chemical Communications, 2022. **58**(39): p. 5901-5904.
36. Utomo, W.P., H. Wu, and Y.H. Ng, *Quantification methodology of ammonia produced from electrocatalytic and photocatalytic nitrogen/nitrate reduction.* Energies, 2022. **16**(1): p. 27.
37. Varghese, A.P., B. Neppolian, and S.K. Lakhera, *Pitfalls of using nessler's reagent for ammonia detection in photocatalytic nitrogen fixation studies: Leveraging 1H NMR for enhanced accuracy and precision.* Industrial & Engineering Chemistry Research, 2023. **62**(32): p. 12530-12537.
38. Peterson, A.A., et al., *How copper catalyzes the electroreduction of carbon dioxide into hydrocarbon fuels.* Energy & Environmental Science, 2010. **3**(9): p. 1311-1315.
39. Niu, H., et al., *Theoretical insights into the mechanism of selective nitrate-to-ammonia electroreduction on single-atom catalysts.* Advanced Functional Materials, 2021. **31**(11): p. 2008533.

40. Lv, L., et al., *Computational screening of high activity and selectivity TM/g-C3N4 single-atom catalysts for electrocatalytic reduction of nitrates to ammonia.* The Journal of Physical Chemistry Letters, 2021. **12**(45): p. 11143-11150.
41. Calle-Vallejo, F., et al., *Theoretical design and experimental implementation of Ag/Au electrodes for the electrochemical reduction of nitrate.* Physical chemistry chemical physics, 2013. **15**(9): p. 3196-3202.
42. Wang, V., et al., *VASPKIT: A user-friendly interface facilitating high-throughput computing and analysis using VASP code.* Computer Physics Communications, 2021. **267**: p. 108033.
43. Momma, K. and F. Izumi, *VESTA 3 for three-dimensional visualization of crystal, volumetric and morphology data.* Journal of applied crystallography, 2011. **44**(6): p. 1272-1276.
44. Tang, W., E. Sanville, and G. Henkelman, *A grid-based Bader analysis algorithm without lattice bias.* Journal of Physics: Condensed Matter, 2009. **21**(8): p. 084204.
45. Das, D., et al., *Phosphine-free avenue to Co 2 P nanoparticle encapsulated N, P co-doped CNTs: a novel non-enzymatic glucose sensor and an efficient electrocatalyst for oxygen evolution reaction.* Green chemistry, 2017. **19**(5): p. 1327-1335.
46. Banipal, T.S., A. Beri, and P.K. Banipal, *Volumetric, viscometric, and 1H NMR studies on caffeine, theophylline, and theobromine in aqueous solutions of MgCl2 at temperatures T=(288.15 to 318.15) K and at pressure p= 101.3 kPa.* Journal of Chemical & Engineering Data, 2017. **62**(11): p. 3833-3847.
47. Chen, M.-T., et al., *Caffeine derived graphene-wrapped Fe3C nanoparticles entrapped in hierarchically porous FeNC nanosheets for boosting oxygen reduction reaction.* Journal of Colloid and Interface Science, 2023. **637**: p. 216-224.